A Comparative Study on Nine- and Twelve-Phase Flux-Switching Permanent-Magnet Wind Power Generators

Lingyun Shao, Wei Hua, Feng Li, Juliette Soulard, Z. Q. Zhu, *Fellow*, *IEEE*, Zhongze Wu, and Ming Cheng, *Fellow*, *IEEE*

***Abstract*—In this paper, two flux-switching permanent-magnet (FSPM) wind power generators with 9- and 12-phase windings are designed and comparatively analyzed. Both two generators are designed under the rated specifications of 10 kW output power and 220 V phase voltage at 500 rpm. The static characteristics and power generating performances including output voltage, power and efficiency at rated and variable load/speed conditions are predicted by finite-element (FE) analysis and validated by experimental tests based on the two FSPM prototypes. It shows that the 12-phase 24-stator-slot/22-rotor-pole FSPM generator exhibits a higher air-gap flux density, a higher torque/power density and a lower voltage regulation factor. Besides, it has a better overload capability than its 9-phase 36-stator-slot/34-rotor-pole counterpart when the load and wind speed exceed the rated levels. The comparative study reveals the benefits of the lower leakage flux and permeance from the larger stator-slot opening and longer magnetic circuit.**

***Index Terms*—9 phase, 12 phase, flux-switching, permanent magnet, switched flux, wind power.**

I. Introduction

THE recent multiphase winding concept for electric machines, including generators and motors, has been proposed for many years due to the advantages of reduced power burden per phase, improved fault-tolerance and additional degrees of freedom. Moreover, the multiphase winding increases the system redundancy, which makes it possible to use modular design and control strategies. The pace of research on multiphase machine systems started accelerating with the rapid development of many safety-critical applications in the early 21st century, such as aerospace, electric vehicles and wind power generation [1]-[4]. The combination of multiphase windings, advanced electric machine topologies and control strategies is a core way to improve the reliability and power density of the whole system [5], [6]. Research area in the multiphase machine has ranged from the design and modelling of novel multiphase machine topologies to the control strategies in normal or fault conditions [7]-[9].

As a novel stator-permanent magnet (PM) machine with both PMs and armature windings located in the stator, flux-switching (FS) PM (FSPM) machines have attracted wide attention due to high flux density, robust rotor and easy PM thermal management [10]-[12]. Reference [13] firstly applies multiphase windings to the FSPM machines for the aero-engine application. The 3-, 4-, 5-, and 6-phase windings are adopted and compared, showing that a higher phase number is beneficial to a lower mutual inductance, and hence a better fault-tolerant performance. A 5-phase FSPM machine presented in [14] employs E-shaped stator laminations to achieve an enhanced fault-tolerant capability. Further, a multiphase modular FSPM wind power generation system is proposed in [15], which adopts twelve 3-phase stator winding segments and twelve paralleled 3-phase converter modules to improve the fault-tolerance and reliability of the energy conversion system.

From the viewpoint of control, an accurate torque model is established in [16] to optimize the reference currents of a 5-phase FSPM machine under short-circuit faulty condition, so as to improve the post-fault operating performance. The open-circuit fault-tolerant control strategy with minimum copper loss for a 9-phase FSPM machine is proposed in [17]. Moreover, reference [18] elaborates a general subdomain model to predict the magnetic field of any FS machine topology with any phase numbers. Compared with the finite-element (FE) method, it greatly saves computational time, but reduces the calculation accuracy of the field tangential component as the soft magnetic material is supposed as linear or with infinite permeability.

In this paper, a comparative study is implemented on two multiphase FSPM wind generators, namely a 9-phase 36-stator-slot/34-rotor-pole (36/34) generator and a 12-phase 24-stator-slot/22-rotor-pole (24/22) generator, as shown in Fig.

Manuscript received January 21, 2019; revised March 22, 2019; accepted March 27, 2019. This work was supported in part by the Shenzhen Science and Technology Project-Basic Research-under Grant JCYJ20170817164652779. and the Fundamental Research Funds for the Central Universities. (*Corresponding author: Wei Hua*.)

Lingyun Shao was with School of Electrical Engineering, Southeast University, Nanjing, 210096, China. She is now with Centre for Automotive Engineering, University of Surrey, Guildford GU2 7XH, U.K. (e-mail: shaolingyun1990@gamil.com).

Wei Hua, Feng Li, and Ming Cheng are with School of Electrical Engineering, Southeast University, Nanjing 210096, China (e-mail: huawei1978@seu.edu.cn; lfeng@ujs.edu.cn; mcheng@seu.edu.cn).

Juliette Soulard is with Warwick Manufacturing Group (WMG), University of Warwick, Coventry CV4 7AL, U.K. (e-mail: j.soulard@warwick.ac.uk).

Z. Q. Zhu is with Department of Electronic and Electrical Engineering, The University of Sheffield, Sheffield S1 4BP, U.K. (e-mail: z.q.zhu@sheffield.ac.uk).

Zhongze Wu is with Department of Mechanical Engineering, University of Bath, Bath BA2 7AY, U.K. (email: z.wu@bath.ac.uk).

1(a) and Fig. 1(b), respectively. The 9-phase FSPM generator has the same dimension as that in [17], while the design process of the 12-phase FSPM wind generator has been introduced in [19]. This paper extends the analysis reported in [20], with additional comparisons between FE results and experimental measurements. Firstly, key differences between generator and motor designs are highlighted and the topologies of the two generators are presented in Section II, in which the influence of the design parameters is analyzed. For the optimized machines, the static characteristics including open-circuit air-gap field, flux-linkage, electromotive force (EMF), cogging torque and static torque under i_d=0 brushless ac (BLAC) operation are comparatively analyzed by FE analysis in Section III. Section IV analyzes the power generating performances of the two generators at both rated condition and variable load/speed operations. Lastly, the experimental tests are implemented on the 9- and 12-phase FSPM prototypes to validate the FE-predicted results in Section V. The comparative study not only makes an all-round investigation on the wind generators' performances, but also gives a guidance for the selection of stator-slot/rotor-pole combinations.

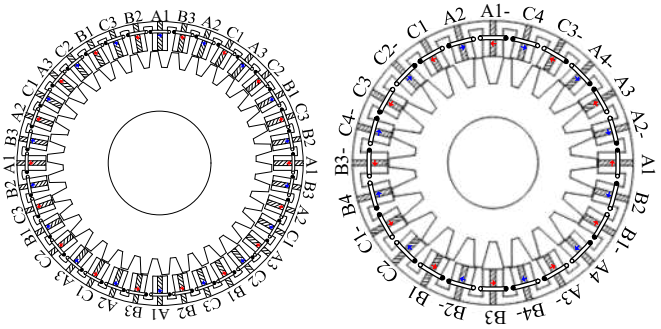

(a) (b)

Fig. 1. Topologies of the 9-phase and 12-phase FSPM generators. (a) 9-phase 36/34 FSPM generator. (b) 12-phase 24/22 FSPM generator.

II. Design of 9- and 12-Phase FSPM Generators

The design procedure of a generator is somewhat different from designing a motor. In most cases, a given point defined by the maximum torque under i_d=0 BLAC operation is focused upon for a motor design. However, for generator applications, the operating mode is determined by the external load. Moreover, the phase angle of the applied armature current is not as controllable as that in a motor. Therefore, it is not rational to optimize a generator under i_d=0 BLAC operation only. Here, a co-simulation method connecting the generator with external circuits is applied to analyze power generating performances.

The stator- and rotor-pole combinations for 9- and 12-phase FSPM generators are determined to achieve a high torque, a low cogging torque and a symmetrical phase EMF waveform [11]. The phase relations of the coil and phase EMF phasors are illustrated in Fig. 2, where the phase shifts between adjacent two phases are 40 and 30 electrical degrees for 9- and 12-phase generators, respectively.

Both generators are designed for a rated power specification of 10 kW and a rated phase voltage of 220 V at rated rotor speed of 500 rpm in [17] and [19]. It should be noted that the two generators are with the same stator outer diameter and stack length as well as the identical PM volume to make a fair comparison. These constraints are remained in this study. The main dimensional parameters of the generators are defined in Fig. 3, where the stator inner radius, stator tooth width, rotor pole width and the number of turns per coil will be optimized with emphasis on the phase EMF and cogging torque in the following parts. The optimized values are given in TABLE I.

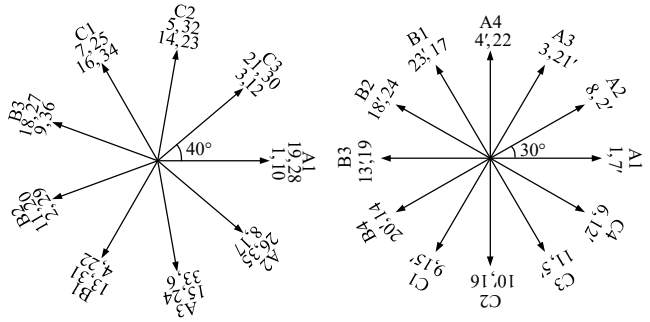

(a) (b)

Fig. 2. Coil and Phase EMF phasors of 9-phase and 12-phase FSPM generators. (a) 9-phase 36/34 FSPM generator. (b) 12-phase 24/22 FSPM generator.

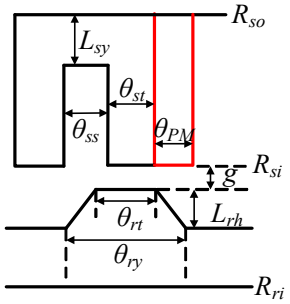

Fig. 3. Linear illustration of main dimensional parameters of FSPM generators.

TABLE I
Main Design Parameters of 9- and 12-Phase FSPM Generators

Item	Unit	9-phase	12-phase
Stator outer diameter, D_{so}	mm	327	
Stator inner diameter, D_{si}	mm	261.6	
Rotor inner diameter, D_{ri}	mm	120	
Effective stack length, L_s	mm	185	
Air-gap length, g	mm	1	
Stator tooth arc, θ_{st}	°	2.625	3.94
PM arc, θ_{PM}	°	2.25	3.375
PM volume	mm^3	89.5×10^4	
Area of each slot	mm^2	217.7	283.1
Rotor pole arc, θ_{rt}	°	3.5	5.25
Number of turns per coil, N_{coil}	-	42	65

A. Stator Inner Radius

Since the stator outer diameter R_{so} is fixed, the stator inner radius R_{si} is proportional to the split ratio, which is defined as the ratio of R_{si} to R_{so}. The split ratio influences the RMS value and total harmonic distortion (THD) of open-circuit phase EMF and the magnitude of cogging torque (T_{cog}) by changing the relation of magnetic and electric loadings.

As can be learned from Fig. 4, the peak points for the EMF and T_{cog} variation curves exist but correspond to different split ratio values. A high magnitude but a low THD of EMF per turn are preferred for a generator, since fewer coil turns would be required to produce the rated voltage specification. Besides, a low cogging torque is favorable for the wind turbine's startup

performance. Therefore, tradeoffs need to be made. The optimization goal is to maximize the RMS value of EMF on the premise of THD<6% and T_{cog}<4 Nm. The optimal split ratio is 0.8 for both generators, since only 0.8 and 0.85 match the requirement of THD [Fig. 4(a)], and cogging torque [Fig. 4(b)].

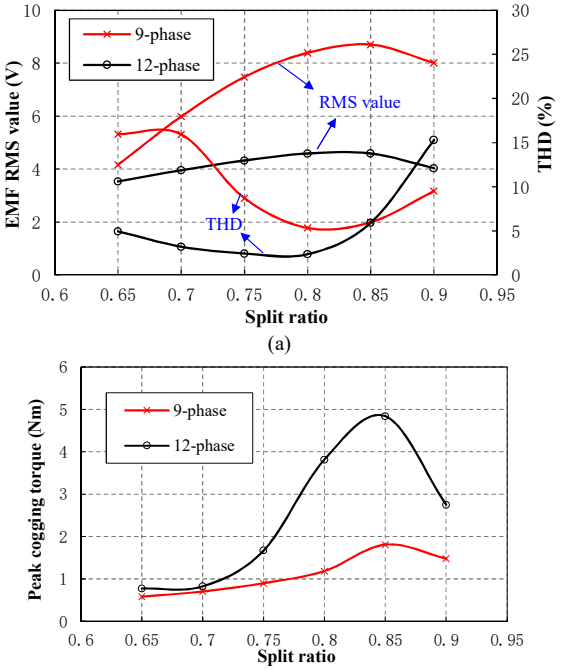

Fig. 4. Influence of split ratio. (a) Phase PM EMF (500 rpm, 1 turn). (b) Cogging torque (Peak value).

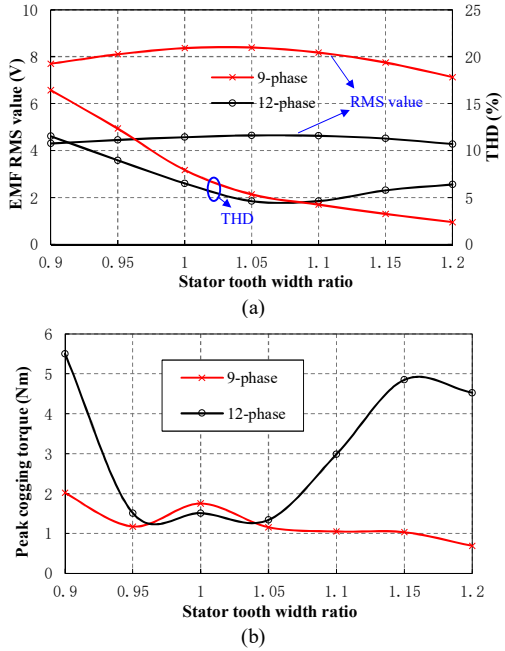

Fig. 5. Influence of stator tooth width. (a) Phase PM EMF (500 rpm, 1 turn). (b) Cogging torque (Peak value).

B. Stator Tooth Width

The stator tooth width ratio is defined as the ratio of stator tooth arc θ_{st} to 1/4 of the stator slot pitch, which influences the cross-sectional area of the effective flux path and tooth-tip leakage by changing the tooth width. Thus, a maximum value exists in the curve of RMS EMF per turn versus stator tooth width, as shown in Fig. 5(a). Luckily, both low THD and T_{cog} are obtained when the phase EMF reaches the peak value. Thus, the optimal stator tooth width ratio is 1.05 for both generators.

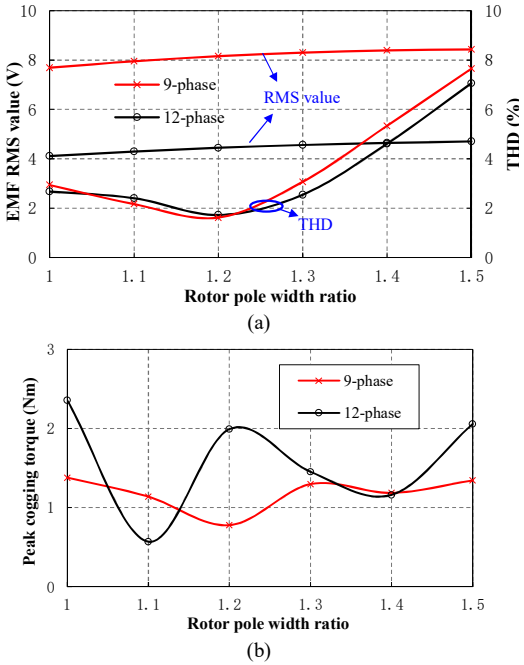

Fig. 6. Influence of rotor pole width. (a) Phase PM EMF (500 rpm, 1 turn). (b) Cogging torque (Peak value).

C. Rotor Pole Width

Similarly, the rotor pole width also has effect on the cross-sectional area of the effective flux path. The rotor pole width ratio is defined as the ratio of rotor pole arc θ_{rt} to 1/4 of the stator slot pitch. As seen from Fig. 6(a), the RMS EMF increases slightly with rotor pole width. The cogging torque magnitude is kept at a low level (T_{cog}<2.5 Nm) during the whole variation range of the rotor pole width (see Fig. 6(b)). For both analysed generators, the optimal rotor pole width is 1.4 for maximization of the EMF under the constraint of THD<6%.

D. Number of Turns Per Coil

Basically, the turn number per coil N_{coil} should be designed to make phase voltage satisfy the rated specification. However, a 20% higher margin is secured to avoid the decrement of voltage caused by manufacture and assembly.

It should be noted that a higher N_{coil} is detrimental to the voltage regulation factor ΔU, which evaluates the generator's voltage stabilization capability when the load changes, as

$$\Delta U = \left(\frac{E_0}{U_o} - 1\right) \times 100\% = \left(\frac{\sqrt{\left(R_N + R_{ph}\right)^2 + {X_s}^2}}{R_N} - 1\right) \times 100\% \quad (1)$$

where E_0 and U_o are the open-circuit EMF and output voltage (RMS values) per phase, respectively. R_N, R_{ph} and X_s are the external resistive load, winding resistance and synchronous

reactance per phase, respectively. The voltage phasor diagram relations are defined in Fig. 7.

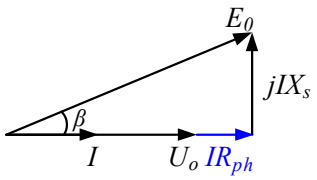

Fig. 7. Simplified voltage phasor diagram of the synchronous generator operating with resistive load R_N (U_o= IR_N).

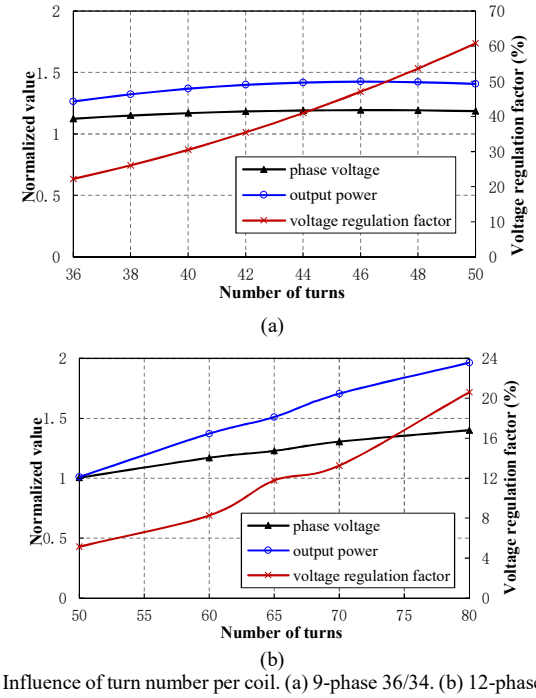

Fig. 8. Influence of turn number per coil. (a) 9-phase 36/34. (b) 12-phase 24/22.

Since R_{ph} is proportional to N_{coil} and reactance X_s is proportional to the square of N_{coil}, the voltage regulation factor definitely increases with the coil turn number as verified in Fig. 8 where the normalized value is calculated based on the rated specification. Besides, the growth rate of E_0 with N_{coil} is much smaller than that of IX_s with N_{coil}, so the reactive power spent on the winding reactance increases fast with the number of coil turns, which would cause the decrease of the output voltage as learned from Fig. 8(a). Consequently, N_{coil} should be restricted for an acceptable voltage regulation factor on the premise of meeting the rated demand.

III. Comparison of Static Characteristics

The static characteristics of the 9- and 12-phase FSPM generators are predicted by FE, including the open-circuit characteristics and on-load torque with the slot current density J_s of 2.5A/mm^2 (RMS value) under i_d=0 BLAC operation.

The open-circuit air-gap radial flux density waveforms are shown in Fig. 9, where the 'local-max' flux density values corresponding to the *d*-axis air-gap flux density [21] are 1.58 T and 1.75 T for the 9- and 12-phase generators, respectively. The phase PM flux-linkage of the 9-phase 36/34 FSPM machine is smaller than that of the 12-phase 24/22 counterpart, as shown in Fig. 10(a). This is caused by a significant leakage flux existing between the adjacent stator teeth in the 9-phase machine, as shown in Fig. 11, due to a smaller stator-slot opening. However, the relationship between EMF magnitudes is opposite to the flux-linkage because of a higher rotor-pole number in the 9-phase machine.

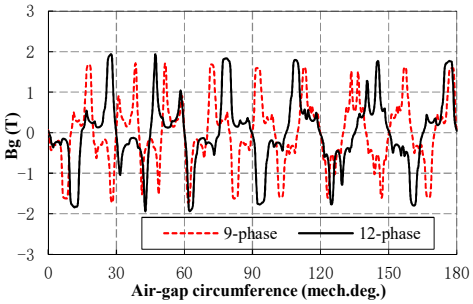

Fig. 9. Open-circuit air-gap radial flux density as function of angular position.

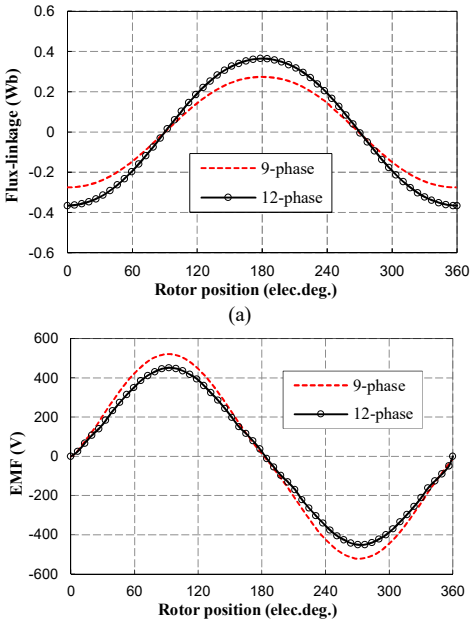

Fig. 10. Open-circuit phase PM flux-linkage and EMF waveforms. (a) Phase PM flux-linkage. (b) Phase EMF (500 rpm).

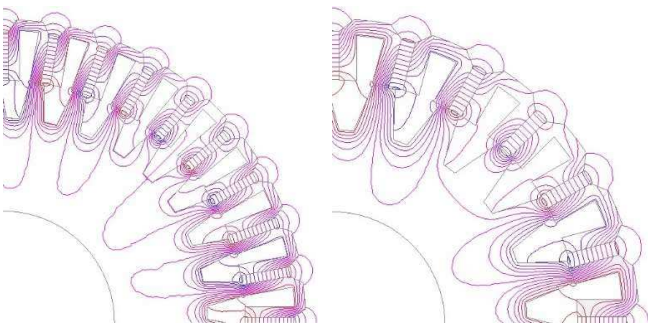

Fig. 11. PM flux lines distributions. (a) 9-phase 36/34. (b) 12-phase 24/22.

The cogging torque and electromagnetic torque are shown in Fig. 12. The torque ripple factor k_{rip} is calculated by (2), where T_{max}, T_{min} and T_{ave} are the maximum torque, minimum torque and average torque, respectively.

$$k_{rip} = \frac{T_{max} - T_{min}}{T_{ave}} \times 100 \qquad (2)$$

The mean values of the electromagnetic torque for the 9- and 12-phase FSPM generators with J_s=2.5A/mm^2 under i_d=0 BLAC operation are 390.7 Nm and 393.8 Nm, respectively. Both generators demonstrate a good starting and low-speed performance with little vibration since the cogging torque and torque ripple are relatively small, as learned from TABLE II.

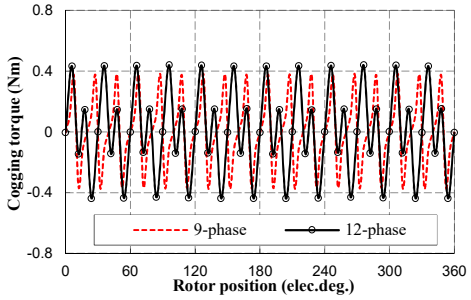

(a)

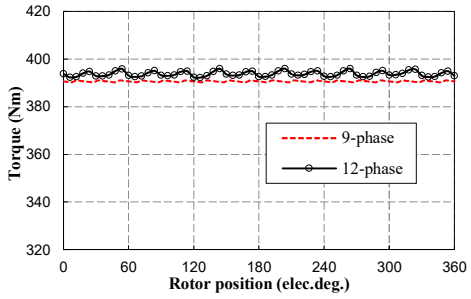

(b)

Fig. 12. Cogging torque and electromagnetic torque waveforms. (a) Cogging torque. (b) Torque (BLAC, i_d=0, J_s=2.5 A/mm^2).

TABLE II
FE-PREDICTED CHARACTERISTICS @500 RPM

Item	Unit	9-phase	12-phase
Open-circuit EMF (rms), E_o	V	364.9	313.6
Rated output voltage (rms), U_o	V	266.2	273.3
Rated output current (rms), I_o	A	6.1	4.7
Rated output power, P_o	kW	14.6	15.6
Rated torque, T_e	Nm	-290.8	-312.8
Torque ripple factor, k_{rip}	%	0.7	0.6
Voltage regulation factor, ΔU	%	37	14.7
$d(q)$-axis inductance, $L_d(L_q)$	mH	19.9 (17.4)	18.6 (19.9)
$d(q)$-axis reactance, $X_d(X_q)$	Ω	35.5 (30.9)	21.5 (23.0)
Phase winding resistance, R_{ph}	Ω	1.59	1.65
Copper loss, p_{Cu}	W	534.4	443.3
Core loss, p_{Fe}	W	301.6	292.8
PM eddy-current loss, p_{ec}	W	57.4	104.7
Efficiency, η	%	94	93

IV. COMPARISON OF POWER GENERATING PERFORMANCES

The generating performances including output voltage, phase current and electromagnetic torque as well as losses of the two generators operated with symmetrical external resistive loads are predicted by FE co-simulation. Then, the output power, voltage regulation factor and efficiency are calculated from the FE-predicted data. The rated resistive load R_N is calculated from the rated power and voltage of each phase. Thus, R_N is 43.6 Ω for the 9-phase generator, while it is 58 Ω for the 12-phase one. Furthermore, the output characteristics of the two generators operating within a load range and a rotor speed range are predicted to evaluate their overload and over-speed capabilities.

A. Rated Performance

The output phase voltages and currents of the 9- and 12-phase generators working at rated generating condition are shown in Fig. 13. Obviously, a higher phase number brings a lower current for each phase under the same power specification, thus helps to mitigate the stator winding loss and overheating problems [2]. Besides, as shown in Fig. 13 and Fig. 14 the 12-phase generator has a higher output voltage, output power and torque than its 9-phase counterpart although with a lower phase current. The reason for the larger output voltage lies in a smaller voltage regulation factor for the 12-phase FSPM generator, as shown in TABLE II. Both generators have a symmetrical voltage waveform with a low THD and a smooth torque with a low torque ripple as in Fig. 13, due to low EMF harmonics and cogging torque. The small overshoot on the torque waveform of the 9-phase machine is caused by the insufficient damping of the small resistance in the circuit.

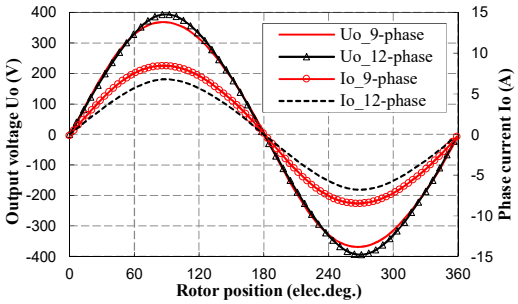

Fig. 13. Output phase voltage and current at rated condition (500 rpm, R_N).

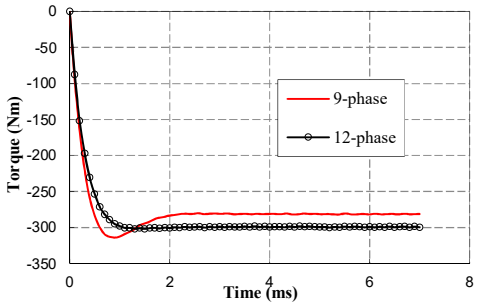

Fig. 14. Electromagnetic torque at rated generating condition (500 rpm, R_N).

B. Overload Capability

The output voltage, current and power of the 9- and 12-phase generators working with different resistive loads at 500 rpm are predicted by FE co-simulation.

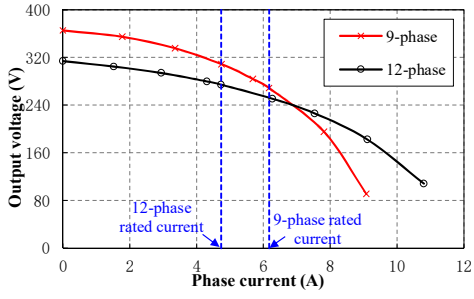

Fig. 15. Output voltage versus phase current (RMS value) @500 rpm.

Fig. 15 shows the variation curves of the output voltage versus phase current. Obviously, the slope of the 9-phase generator's curve is greater than that of the 12-phase counterpart, indicating a greater voltage variation when the load changes in the 9-phase FSPM generator. This means the 12-phase FSPM generator is more advantageous than the 9-phase counterpart in terms of maintaining a stable output voltage. Fig. 16 illustrates the variation curves of the output power versus phase current, which indicates the overload capability of the generators. The maximum points' coordinates of the two curves are (6.2 A, 15 kW) and (8.3 A, 20.4 kW) for the 9- and 12-phase generators, respectively. Referring to their rated points, the maximum output power is quite close to the rated power in the 9-phase generator, while it is 1.3 times of the rated value in the 12-phase generator. Clearly, the 12-phase FSPM generator has a better overload capability. However, the 9-phase generator has a higher efficiency when the phase current is lower than 9 A, as shown in Fig. 17, due to a smaller eddy-current loss in the PMs.

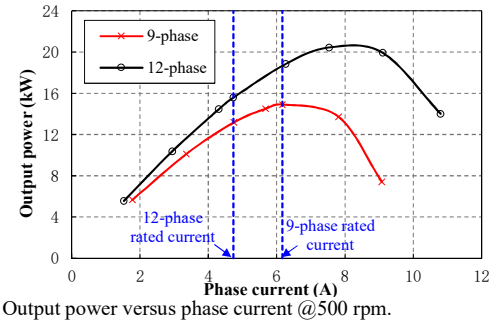

Fig. 16. Output power versus phase current @500 rpm.

The great difference on the overload capability between the two generators is caused by the distinct winding reactance. The *d*/*q*-axis inductance and the corresponding reactance are calculated as shown in TABLE II, by taking the *d*- and *q*-axis cross-coupling into account [22]. The reactance of the 9-phase FSPM generator is much larger than another one, due to a higher rotor-pole number. Therefore, the reactive power spent on the winding reactance increases a lot even though the phase current grows slightly, which brings a large drop in the output voltage and prevents the output power from increasing.

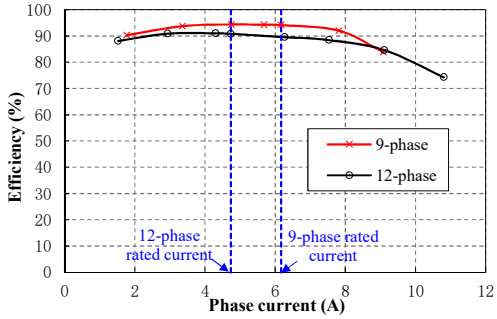

Fig. 17. Efficiency versus phase current @500 rpm.

C. *Variable Speed Performances*

The electromagnetic torque in Fig. 18 "saturates" with the rotor speed increment. Besides, when the speed rises to a certain value, the torque may start to decrease due to the decline of the *q*-axis current, since the load angle between the open-circuit EMF and phase current also increases with the rotor speed. The growth rate of the load angle is related to the winding reactance. The higher the reactance, the faster the load angle increases, as learned from Fig. 7. Thus, the torque of the 9-phase generator is more easily to get saturated and then decrease with the rise of the rotor speed. This applies equally to the output power shown in Fig. 19.

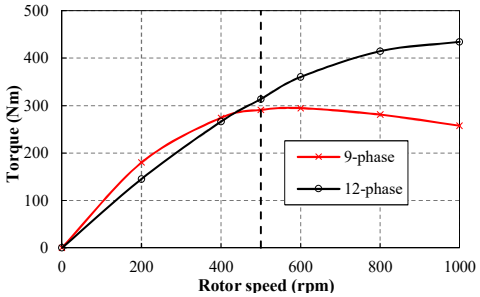

Fig. 18. Torque versus rotor speed of the generators connected with R_N.

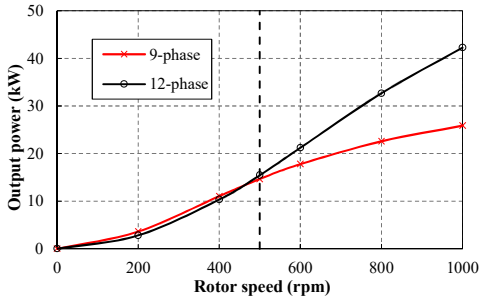

Fig. 19. Output power versus rotor speed of the generators connected with R_N.

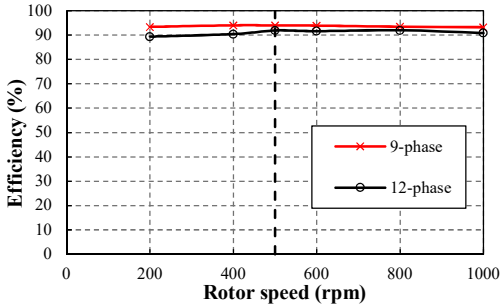

Fig. 20. Efficiency versus rotor speed of the generators connected with R_N.

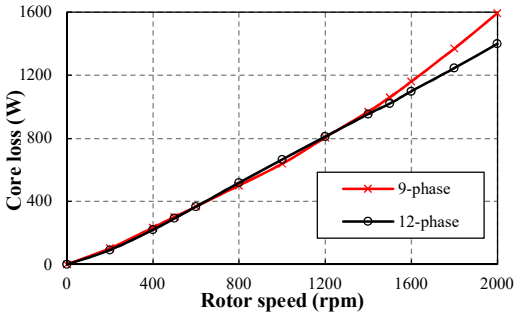

Fig. 21. Core loss versus rotor speed of the generators connected with R_N.

Fig. 20 and Fig. 21 show the efficiency and core loss variation with the speed, respectively. The core losses of the two machines at low speeds are close to each other due to the compensation between flux density and electric frequency. However, when the rotor speed grows over 1200 rpm, the core loss of the 9-phase machine begins to surpass the 12-phase counterpart and the difference gets greater with the increase of rotor speed, due to the higher rotor pole number. The efficiency

of the two generators hardly changes within 200-1000 rpm. However, it should be noted that the winding current increases greatly with the rotor speed, so a better cooling condition is needed in high-speed operation.

V. Experimental Validation

To verify the FE predicted results, two FSPM prototypes with 12-phase 24-stator-slot/22-rotor-pole and 9-phase 36-stator-slot/34-rotor-pole combinations are manufactured as shown in Fig. 22 and Fig. 23, respectively. The two prototypes have the same stator outer diameter and stack length as well as identical core and PM material properties. The test bench including a DC motor, an FSPM prototype generator, the variable resistance, the shaft coupling and a torque sensor as shown in Fig. 24 is set up for the implementation of the open-circuit and on-load power generating experiments.

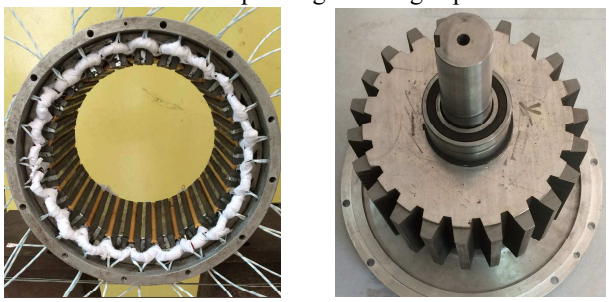

(a) (b)

Fig. 22. Prototype of the 12-phase 24/22 FSPM machine. (a) Stator. (b) Rotor.

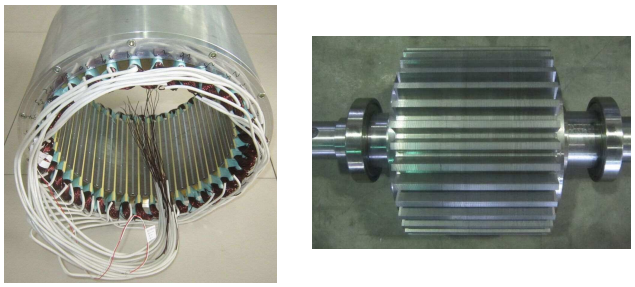

(a) (b)

Fig. 23. Prototype of the 9-phase 36/34 FSPM machine. (a) Stator. (b) Rotor.

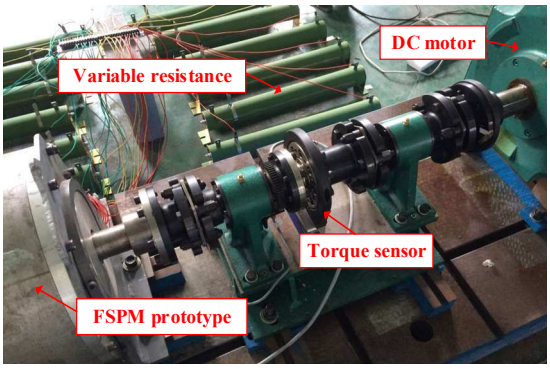

Fig. 24. Test bench of the 9- and 12-phase FSPM prototypes.

A. Open-Circuit Test

As shown in Fig. 25, the measured phase fundamental RMS EMFs for two generators are 308 V and 271 V, respectively, as shown in TABLE III. The measured results for the 9- and 12-phase generators are 15% and 13% lower than the FE-predicted results, respectively, which is mainly caused by the end effect and lamination stacking factor.

B. On-Load Test

The on-load experiments are implemented on each prototype which is connected to the variable resistance and driven by a DC motor at 500 rpm. The resistive load is adjusted to 43.6 Ω for the 9-phase generator, while 58 Ω for the 12-phase one, to establish the rated power generating condition. The output voltage waveforms of each phase for the 9- and 12-phase FSPM generators are measured as shown in Fig. 26(a) and (b), respectively. Meanwhile, the torque waveforms are measured and compared with the FE-predicted results as shown in Fig. 27. The RMS value of the phase voltage, the average mechanical torque and the calculated test results including output power, voltage regulation factor and efficiency are listed in TABLE III. It can be learned that the measured results are consistent with the FE predictions, although with the differences of 11% and 8% for 9- and 12-phase prototypes due to manufacturing and measurement errors.

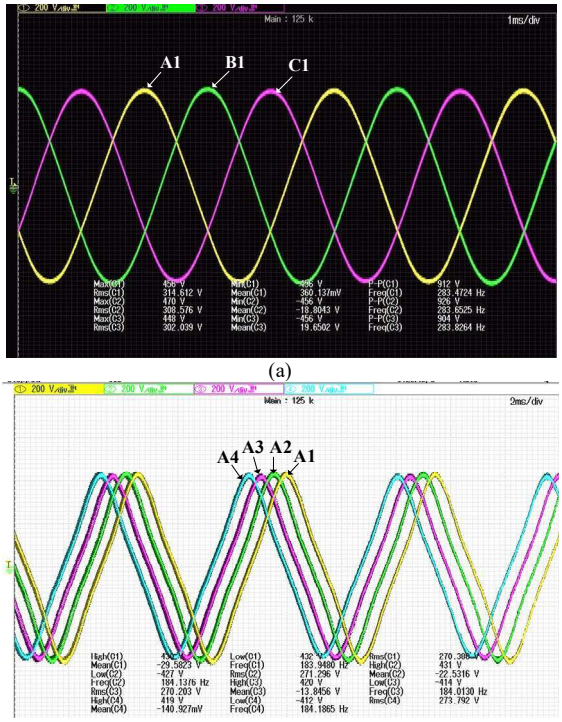

(a)

(b)

Fig. 25. Measured open-circuit phase EMF waveforms @ 500rpm. (a) 9-phase 36/34 FSPM generator. (b) 12-phase 24/22 FSPM generator.

TABLE III
Measured Results of The Two FSPM Generators @500 rpm

Item	Unit	9-phase	12-phase
Open-circuit phase EMF (rms), E_o	V	308	271
Rated phase voltage (rms), U_o	V	222	223
Rated phase current (rms), I_o	A	4.9	3.9
Rated output power, P_o	kW	9.8	10.3
Input mechanical torque, T_i	Nm	210	230.4
Voltage regulation factor, ΔU	%	38.7	22
Efficiency, η	%	89	87.8

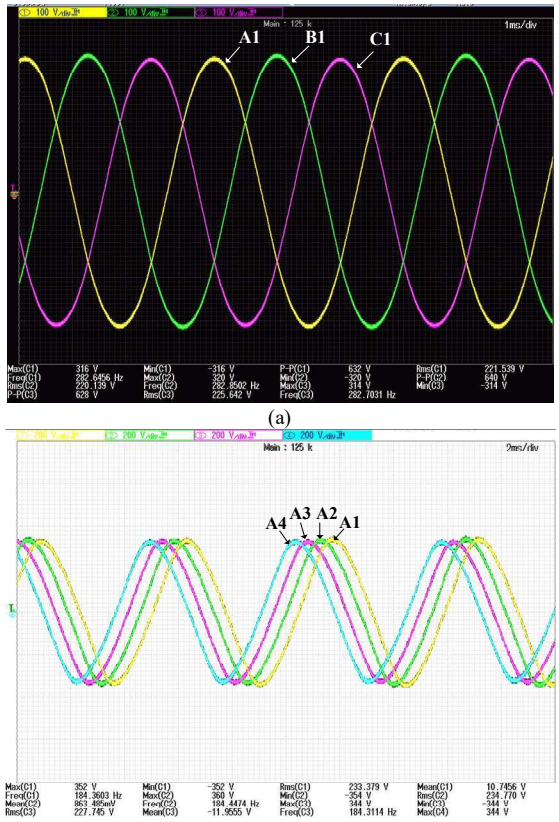

(a)

(b)

Fig. 26. Measured phase voltage waveforms of prototypes connected with rated resistive load @500rpm. (a) 9-phase. (b) 12-phase.

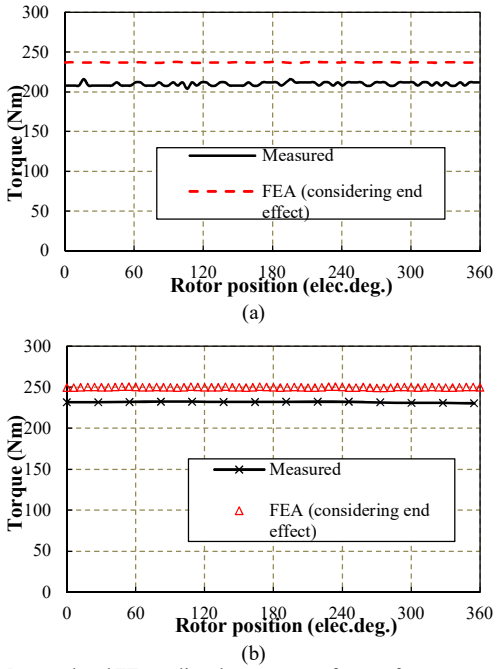

(a)

(b)

Fig. 27. Measured and FE-predicted torque waveforms of prototypes connected with rated resistive load @500rpm. (a) 9-phase. (b) 12-phase.

VI. Conclusion

This paper compares the performances of the 9-phase 36/34 and 12-phase 24/22 FSPM machines designed for wind power generation. The results show that the 12-phase generator has a higher power density, a lower voltage regulation factor and a stronger overload/over-speed capability than the 9-phase counterpart. It also indicates that a high pole number may not be preferred for a small-scale FSPM wind generator, since it causes higher leakage flux, magnetic circuit permeance and winding reactance, although it brings lower cogging torque and torque ripple. Therefore, more stator- and rotor-pole combinations will be studied in the future, e.g. 18/16 and 18/17 may be good choices for the 9-phase machine with larger slot openings. The slot opening width can also be optimized to reduce the leakage flux between adjacent two stator teeth, thus, to reduce the leakage inductance. To improve the performances, further work will also be carried out on the magnetic path optimization to balance the magnetic flow and the magnetic permeance, since both a high magnetic flow for a large torque and a low permeance for a high power factor are preferred. The FE predicted performances and analyzed results are validated by experimental tests based on two FSPM prototypes.

References

[1] E. Levi, "Multiphase electric machines for variable-speed applications," *IEEE Trans. Ind. Electron*., vol. 55, no. 5, pp. 1893–1909, May 2008.

[2] S. Williamson, S. Smith, and C. Hodge, "Fault tolerance in multiphase propulsion motors," *J. Mar. Eng. Technol*., vol. 3, no. 1, pp. 3-7, 2004.

[3] L. Parsa, "On advantage of multiphase machines," in *Proc. of Conf. of IEEE Ind. Electron. Soc*., Raleigh, USA, pp. 1574-1579, 2005.

[4] S. Brisset, D. Vizireanu, and P. Brochet, "Design and optimization of a nine-phase axial-flux PM synchronous generator with concentrated winding for direct-drive wind turbine," *IEEE Trans. Ind. Appl*., vol. 44, no. 3, pp. 707-715, May/June 2008.

[5] F. Barrero, and M. J. Duran, "Recent advances in the design, modeling and control of multiphase machines—Part I," *IEEE Trans. Ind. Electron*., vol. 63, no. 1, pp. 449–458, Jan. 2016.

[6] M. J. Duran, and F. Barrero, "Recent advances in the design, modeling and control of multiphase machines—Part II," *IEEE Trans. Ind. Electron*., vol. 63, no. 1, pp. 459–468, Jan. 2016.

[7] A. Labak, and N. C. Kar, "Designing and prototyping a novel five-phase pancake-shaped axial-flux SRM for electric vehicle application through dynamic FE incorporating flux-tube modeling," *IEEE Trans. Ind. Appl*., vol. 49, no. 3, pp. 1276-1288, May/June 2013.

[8] M. Bermudez, I. Gonzalez-Prieto, F. Barrero, H. Guzman, M. J. Duran, and X. Kestelyn, "Open-phase fault-tolerant direct torque control technique for five-phase induction motor drives," *IEEE Trans. Ind. Electron*., vol. 64, no. 2, pp. 902–911, Feb. 2017.

[9] A. Mohammadpour, and L. Parsa, "Global fault-tolerant control technique for multiphase permanent-magnet machines," *IEEE Trans. Ind. Appl*., vol. 51, no. 1, pp. 178-186, Jan./Feb. 2015.

[10] Z. Q. Zhu, and J. T. Chen, "Advanced flux-switching permanent magnet brushless machines," *IEEE Trans. Magn*., vol. 46, no. 6, pp. 1447–1453, Jun. 2010.

[11] Z. Z. Wu, and Z. Q. Zhu, "Analysis of air-gap field modulation and magnetic gearing effects in switched flux permanent magnet machines," *IEEE Trans. Magn*., vol. 51, no. 5, pp. 1–12, May 2015, Art. ID 8105012.

[12] J. Ojeda, M. G. Simoes, G. Li, and M. Gabsi, "Design of a flux-switching electrical generator for wind turbine systems," *IEEE Trans. Ind. Appl*., vol. 48, no. 6, pp. 1808–1816, Nov./Dec. 2012.

[13] A. S. Thomas, Z. Q. Zhu, R. L. Owen, G. W. Jewell, and D. Howe, "Multiphase flux-switching permanent-magnet brushless machine for aerospace application," *IEEE Trans. Ind. Appl*., vol. 45, no. 6, pp. 1971–1981, Nov./Dec. 2009.

[14] X. Xue et al., "Design of five-phase modular FSPM machines for high reliability applications," *IEEE Trans. Magn*., vol. 49, no. 7, pp. 3941–3944, Jul. 2013.

[15] C. Ditmanson, P. Hein, S. Kolb, J. Molck, and S. Bernet, "A new modular flux-switching permanent magnet drive for large wind turbines," *IEEE Trans. Ind. Appl*., vol. 50, no. 6, pp. 3787–3794, Nov./Dec. 2014.

[16] E. B. Sedrine, J. Ojeda, M. Gabsi, and I. Slama-Belkhodja, "Fault-tolerant control using the GA optimization considering the reluctance torque of a five-phase flux switching machine," *IEEE Trans. Energy Convers*., vol. 30, no. 3, pp. 927–938, Sept. 2015.
[17] F. Li, W. Hua, M. Cheng, and G. Zhang, "Analysis of fault tolerant control for a nine-phase flux-switching permanent magnet machine," *IEEE Trans. Magn*., vol. 50, no. 11, pp. 1–4, Nov. 2014, Art. ID 14787235.
[18] K. Boughrara, T. Lubin, and R. Ibtiouen, "General subdomain model for predicting magnetic field in internal and external rotor multiphase flux-switching machines topologies," *IEEE Trans. on Magn*., vol. 49, no. 10, pp. 5310–5325, 2013.
[19] L. Shao, W. Hua, and M. Cheng, "Design of a twelve-phase flux-switching permanent magnet machine for wind power generation," in *Proc. of Int. Conf. on Elec. Mach. and Syst*., Hangzhou, China, pp. 435–441, 2014.
[20] L. Shao, W. Hua, F. Li, J. Soulard, Z. Q. Zhu, Z. Wu, and M. Cheng, "A comparative study on nine- and twelve-phase flux-switching permanent-magnet wind generators," in *Proc. of Conf. of IEEE Energy Conversion Congress and Exposition*, Portland, USA, pp. 4283-4289, Sept. 2018
[21] W. Hua, G. Zhang, and M. Cheng, "Flux-regulation theories and principles of hybrid-excited flux-switching machines," *IEEE Trans. Ind. Electron*., vol. 62, no. 9, pp. 5359–5369, Sep. 2015.
[22] G. Qi, J. T. Chen, Z. Q. Zhu, D. Howe, L. Zhou, and C. Gu, "Influence of skew and cross-coupling on flux-weakening performance of permanent magnet brushless AC machines," *IEEE Trans. Magn*., vol. 45, no. 5, pp. 2110–2117, May 2009.

Lingyun Shao was born in Jiangsu, China, in 1990. She received the B.Sc. and Ph.D. degrees in electrical engineering from the School of Electrical Engineering, Southeast University, Nanjing, China, in 2012 and 2018, respectively.

Since January 2019, she has been with Centre for Automotive Engineering, Department of Mechanical Engineering Sciences, University of Surrey, Guildford, U. K., where she is currently a research fellow in electric motor simulation and optimization. Her current research interests include the design and analysis of permanent magnet machines for electric propulsion systems and renewable energy generation.

From December 2015 to December 2016, she was also with the Department of Electronic and Electrical Engineering, The University of Sheffield, Sheffield, U.K., as a joint PhD student, sponsored by China Scholarship Council (CSC). From July 2017 to December 2017, she was also with the Warwick Manufacturing Group (WMG), University of Warwick, Coventry, U.K., as a visiting research student.

Wei Hua (SM'16) received B.Sc. and Ph.D. degrees in electrical engineering from the School of Electrical Engineering, Southeast University, Nanjing, China, in 2001 and 2007, respectively.

Since 2007, he has been with Southeast University, where he is currently a Professor with the School of Electrical Engineering. He is the author or coauthor of over 140 technical papers, and he is the holder of 30 patents in his areas of interest. His teaching and research interests include the design, analysis, and control of electrical machines.

Feng Li received the B.Sc. and M.Sc. degrees in electrical engineering from Jiangsu University, Zhenjiang, China, in 2004 and 2008, respectively, and the Ph.D. degree in electrical engineering from Southeast University, Nanjing, China, in 2018.

Since 2004, he has been with Jiangsu University, where he is currently a Lecturer in the College of Electronic and Information Engineering. His research interests include electric machine design, modeling, and control.

Juliette Soulard (M'00) received her Ph.D. degree in electrical engineering from the University of Paris VI, France, in 1998. From 1999 to 2016, she led research on electric machines for industrial applications at the KTH Royal Institute of Technology, Stockholm, Sweden, in close collaboration with the Swedish industry. Since 2016, she has been an Associate Professor with the Warwick Manufacturing Group, University of Warwick, Coventry, United Kingdom.

Her current research activities are focused on accounting for manufacturing effects in modeling and design of permanent-magnet synchronous machines used in advanced propulsion systems.

Z. Q. Zhu (M'90–SM'00–F'09) received the B.Eng. and M.Sc. degrees in electrical and electronic engineering from Zhejiang University, Hangzhou, China, in 1982 and 1984, respectively, and the Ph.D. degree in electrical and electronic engineering from The University of Sheffield, Sheffield, U.K., in 1991.

Since 1988, he has been with The University of Sheffield, where he is currently a Research Chair of the Royal Academy of Engineering/Siemens with the Department of Electronic and Electrical Engineering and the Head of the Electrical Machines and Drives Research Group. His current research interests include the design and control of permanent-magnet brushless machines and drives for applications ranging from automotive through domestic appliances to renewable energy.

Dr. Zhu is a Fellow of the Royal Academy of Engineering.

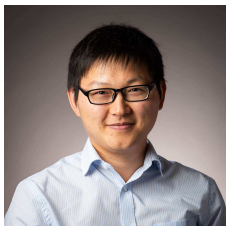

Zhongze Wu (M'18) received the B.Eng. and M.Sc. degrees in electrical engineering from Southeast University, Nanjing, China, in 2010 and 2013, respectively, and the Ph.D. degree in electrical and electronic engineering from The University of Sheffield, Sheffield, U.K., in January 2017.

Since August 2018, he has been with the Powertrain and Vehicle Research Centre, Department of Mechanical Engineering, University of Bath, Bath, U.K., where he is currently a Prize Fellow in Electric Propulsion. His major research interests include the advanced electrical machines and drives for electric propulsion systems.

From January 2017 to August 2018, he was with the Warwick Manufacturing Group (WMG), University of Warwick, Coventry, U.K., as a research fellow in electrical machines.

Ming Cheng (M'01–SM'02–F'15) received the B.Sc. and M.Sc. degrees in electrical engineering from Southeast University, Nanjing, China, in 1982 and 1987, respectively, and the Ph.D. degree in electrical and electronic engineering from the University of Hong Kong, Hong Kong, in 2001.

Since 1987, he has been with Southeast University, where he is currently a Distinguished Professor in the School of Electrical Engineering and the Director of the Research Center for Wind Power Generation. From January to April 2011, he was a Visiting Professor at the Wisconsin Electric Machine and Power Electronics Consortium, University of Wisconsin, Madison, WI, USA. He has authored or co-authored more than 300 technical papers and four books, and is the holder of 55 patents in his research areas. His teaching and research interests include electrical machines, motor drives for electric vehicles, and renewable energy generation.

Prof. Cheng is a fellow of the Institution of Engineering and Technology. He has served as the Chair and Organizing Committee Member for many international conferences. He was a Distinguished Lecturer of the IEEE Industry Applications Society in 2015/2016.